Measuring heat flux from collective Thomson scattering with non-Maxwellian distribution functions

Cite as: Phys. Plasmas **26**, 032104 (2019); https://doi.org/10.1063/1.5086753
Submitted: 22 December 2018 . Accepted: 04 February 2019 . Published Online: 14 March 2019

R. J. Henchen, M. Sherlock, W. Rozmus, J. Katz, P. E. Masson-Laborde, D. Cao, J. P. Palastro, and D. H. Froula

Physics of Plasmas ARTICLE scitation.org/journal/php

Measuring heat flux from collective Thomson scattering with non-Maxwellian distribution functions

Cite as: Phys. Plasmas **26**, 032104 (2019); doi: 10.1063/1.5086753
Submitted: 22 December 2018 · Accepted: 4 February 2019 ·
Published Online: 14 March 2019

R. J. Henchen,[1,2,a)] M. Sherlock,[3] W. Rozmus,[4] J. Katz,[1] P. E. Masson-Laborde,[5] D. Cao,[1] J. P. Palastro,[1] and D. H. Froula[1,6,b)]

AFFILIATIONS

[1]Laboratory for Laser Energetics, University of Rochester, 250 East River Road, Rochester New York 14623, USA
[2]Department of Mechanical Engineering, University of Rochester, Rochester New York 14623, USA
[3]Lawrence Livermore National Laboratory, Livermore, California 94551, USA
[4]Department of Physics, University of Alberta, Edmonton, Alberta T6G 2E1, Canada
[5]CEA, DAM, DIF, F-91297 Arpajon Cedex, France
[6]Department of Physics and Astronomy, University of Rochester, Rochester New York 14623, USA

Note: This paper is part of the Special Collection: Papers from the 60th Annual Meeting of the APS Division of Plasma Physics.
Note: Paper QI3 4, Bull. Am. Phys. Soc. **63** (2018).
[a)]Invited speaker.
[b)]**Electronic mail:** dfroula@lle.rochester.edu

ABSTRACT

Heat flux was measured in coronal plasmas using collective Thomson scattering from electron-plasma waves. A laser-produced plasma from a planar aluminum target created a temperature gradient along the target normal. Thomson scattering probed electron-plasma waves in the direction of the temperature gradient with phase velocities relevant to heat flux. The heat-flux measurements were reduced from classical values inferred from the measured plasma conditions in regions with large temperature gradients and agreed with classical values for weak gradients. In regions where classical theory was invalid, the heat flux was determined by reproducing the measured Thomson-scattering spectra using electron distribution functions consistent with nonlocal thermal transport. Full-scale hydrodynamic simulations using both flux-limited thermal transport (*FLASH*) and the multigroup nonlocal Schurtz, Nicolaï, and Busquet models underestimated the heat flux at all locations.

I. INTRODUCTION

Thermal transport in plasmas is of particular interest to inertial confinement fusion, where a correct description of heat flux is crucial for modeling the absorption of incident laser beams used to implode fusion targets.[1–4] Electron thermal transport is a fundamental process in plasma physics which becomes difficult to calculate since even in the most-modest conditions, classical theory tends to break down. Extensive work[5–19] has attempted to determine the nonlocal heat flux that is responsible for transporting thermal energy over large distances, but quantitative experiments are required.

In laser-produced plasmas, where energy is primarily deposited locally at critical density, temperature gradients inherently drive non-Maxwellian electron distribution functions as electrons carry the heat down the temperature gradient and slower electrons carry a return current up the temperature gradient to maintain neutrality. Classical theory, first developed by Spitzer–Härm,[20] includes a first-order correction to the 3-D Maxwellian electron distribution function

$$f_e^{3D}(\mathbf{v}) = f_0^{3D}(\mathbf{v}) + \frac{\lambda_{ei}}{L_T} f_1^{3D}(\mathbf{v}), \tag{1}$$

where the amplitude of the correction is given by the ratio of the electron–ion mean free path (λ_{ei}) to temperature scale length ($L_T = T_e/\nabla T_e$), $f_1^{3D}(v) = \sqrt{2/9\pi}(\mathbf{v}/v_{te})^4(4 - \mathbf{v}^2/2v_{te}^2) f_0^{3D}(\mathbf{v}) \cos\theta$, $f_0^{3D}(\mathbf{v}) = n_e \exp(-v^2/2v_{te}^2)/(2\pi)^{3/2} v_{te}^3$, $v_{te} = \sqrt{T_e/m_e}$ is the thermal velocity, and θ is the angle between the electron velocity and the temperature gradient. The heat flux reduces to the well-known classical result when integrating the third velocity moment

$$\mathbf{q} = \int \frac{1}{2} m_e v^2 \mathbf{v} f_e^{3D}(\mathbf{v}) d^3v = -\kappa \nabla T_e, \quad (2)$$

where κ is the classical thermal conductivity that depends only on the local electron temperature and density. Classical theory breaks down when the amplitude of the first-order correction ($\lambda_{ei}/|L_T| \simeq 7 \times 10^{-3}$) becomes larger than the zero-order Maxwellian distribution at velocities where most of the heat-carrying electrons are present ($\sim$3.5 v_{te}). Physically, this failure of classical theory results from the mean free path of the heat-carrying electrons exceeding the temperature scale length. More computationally expensive methods of calculating the heat flux have been developed,[6,13,21,22] including the Schurtz, Nicolaï, and Busquet (SNB)[17] model, which accounts for the velocity-dependent mean free path of electrons.

A consequence of heat flux, and the ensuing distortion of the distribution function, is to change the partition of energy between the thermal electrons and the thermal fluctuations. This has a particularly large effect on the amplitude of the fluctuations that have phase velocities near the velocity of the heat-carrying electrons. The heat flux modifies both the number of electrons and the slope of the distribution function, which directly changes the local Landau damping of ion-acoustic and Langmuir waves. For ion-acoustic waves in plasmas with small ion Landau damping, these changes can lead to an unstable fluctuation spectrum, for example, in the case of return current instability.[23–27]

Collective Thomson scattering measures the fluctuation spectrum, and when probing electron-plasma fluctuations with phase velocities in the region of heat-carrying electrons, the spectrum can be used to determine the heat flux.[12] When probing the ion-acoustic fluctuations, the return current can be probed.[28] Figure 1 shows the corresponding effects to the amplitude of the Thomson-scattering spectrum in the presence of heat flux. Furthermore, measuring the frequencies of the electron-plasma wave and ion-acoustic wave resonances provides measurements of the local plasma conditions.[11,23,29–31] Historically, these measured plasma conditions have been compared with hydrodynamic simulations to study the integrated effects of thermal transport,[9,11,30,32] and recently, collective Thomson scattering was used to directly measure the heat flux.[12]

In this paper, we present the direct measurement of heat flux using collective Thomson scattering from laser-produced coronal plasmas. The heat flux was measured in two ways which were used to experimentally determine the validity of classical thermal transport. The first measurement of heat flux varied the amplitude of the first-order correction (λ_{ei}/L_T) in the classically derived non-Maxwellian electron distribution functions [Eq. (1)] to reproduce the electron-plasma wave Thomson-scattering spectra, while the second method used the measured plasma conditions to calculate the classical heat flux [Eq. (2)]. The plasma conditions used in Eq. (2) were determined by measuring the electron-plasma wave resonant frequency and its width, which provided the spatially resolved temperature (T_e) and density (n_e) along the temperature gradient. In regions with small relative temperature gradients ($\lambda_{ei}/|L_T| < 7 \times 10^{-3}$), the two heat-flux measurements agreed, demonstrating the validity of the classical Spitzer–Härm theory. For larger relative temperature gradients, the flux determined from non-Maxwellian electron distribution functions derived from classical theory was not consistent with the heat flux determined from measurements of the plasma conditions. This experimentally demonstrated that in plasmas with steep relative temperature gradients, the classical thermal transport theory is not valid. To determine the flux in this region, non-Maxwellian electron distribution functions consistent with nonlocal thermal transport were used to fit the Thomson-scattering spectra. At the steepest relative temperature gradient, the nonlocal heat-flux measurements were up to 2× smaller than the flux determined from classical theory [Eq. (2)]. One-dimensional calculations using the SNB model,[17] initiated with the measured plasma conditions, show a reduced heat flux compared to the classical theory but overestimated the flux at all locations compared to the nonlocal measurements. Full radiation hydrodynamic simulations[33] that incorporate the SNB thermal transport model underpredict the heat flux at all measured locations.

In the following sections, the experimental configurations are presented (Sec. II); the Thomson-scattering measurements are discussed (Sec. III); the results of the classical and nonlocal measurements are presented (Sec. IV); and the full-scale integrated radiation hydrodynamic simulations of the experiments are presented (Sec. V).

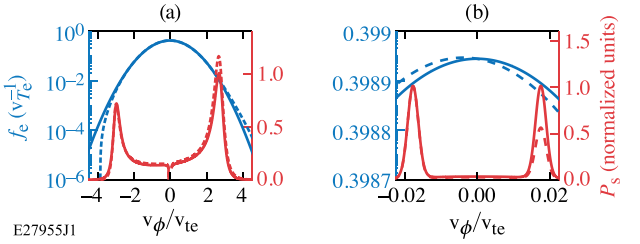

FIG. 1. Calculated Thomson-scattering features (orange, right axis) from (a) electron-plasma waves and (b) ion-acoustic waves are shown ($v_\phi = \omega/k$) using a Maxwellian (solid blue, left axis) and non-Maxwellian (dashed blue) electron distribution function that accounts for classical Spitzer–Härm heat flux ($\lambda_{ei}/|L_T| = 2.2 \times 10^{-3}$, $q/q_{FS} = 3\%$).

II. EXPERIMENTAL CONFIGURATION

A. Laser/target

The experiments were performed on the OMEGA[34] Laser System at the University of Rochester's Laboratory for Laser Energetics using six 351-nm laser beams with equal energies for a total of 1.5 kJ which was delivered in a 2-ns square pulse. The beam profiles on the target were shaped with distributed phase plates[35] to be a high-order super Gaussian ($n = 4.6$) with a full width at half maximum of 560 μm. Figure 2 shows the experimental setup where the incident angle of the beams (8°, 29°, 32°, 33°, 35°, and 40°) was minimized. The aluminum targets were 3 mm × 3 mm × 0.1 mm. The target normals were aligned with the wave vectors that were probed using Thomson scattering.

B. Thomson-scattering diagnostic

The Thomson-scattering diagnostic[36] used a 40-J, 2-ns-long, $\lambda_{2\omega}$ = 526.5-nm probe beam with a best-focus diameter of $\sim$50 μm.[37] The light scattered from a 50 × 50 × 50-μm volume and at an angle of 120° with respect to the probe beam was split into legs that used spectrometers with a low- and high-spectral resolving power to measure the electron-plasma and ion-acoustic wave features, respectively. The low-resolving power system used a 1/3-m spectrometer with a spectral dispersion of 0.411 nm/pxl ± 0.4% to create a spectral window of approximately 300 nm and a resolution of 0.5 nm, while the high-

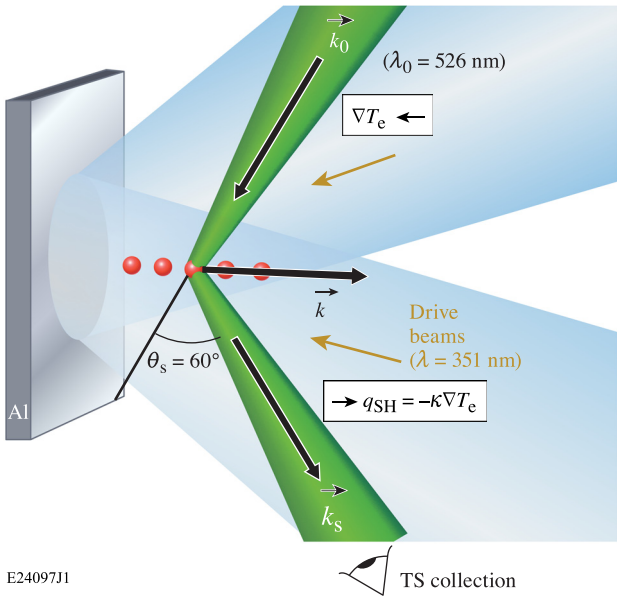

FIG. 2. The experimental setup is shown where six beams (blue) produced a blow-off plasma from a planar target (gray). A Thomson-scattering probe beam (green) with wave vector $\mathbf{k}_0$ was oriented relative to the target to probe plasma waves ($\mathbf{k}$) along the central axis, where the temperature gradient is the largest. Five Thomson-scattering locations (red) along the target normal provided measurements of plasma parameter profiles (T_e, n_e, and ∇T_e).

resolving system used a 1-m spectrometer to obtain a spectral dispersion of 0.00568 nm/pxl ± 0.6% over a 4-nm spectral window and a spectral resolution of 0.05 nm. The temporal resolution of both systems was dominated by the pulse-front tilt introduced by the spectrometers[38] and was 20 ps and 100 ps for the 1/3-m and 1-m systems, respectively. The scattering volume was positioned at five different locations along the target normal ranging from 1.1 mm to 1.5 mm from the initial target surface (Fig. 2).

Experimental effects, including the spectral instrument function and the finite wave vectors introduced by the numerical apertures of the optics, broadened the Thomson-scattering spectrum. These effects were negligible for electron-plasma wave features, but they had a significant effect on the ion-acoustic features. The range of wave vectors created by the finite-diameter lenses used to focus the probe beam ($f^{\#}_{probe} = 6.7$) and collect the Thomson-scattered light ($f^{\#}_{col} = 10$) created an asymmetry in the amplitudes of the ion-acoustic wave features.[39] This asymmetry resulted from the different frequency shifts of the red- (ω_-) and blue-shifted (ω_+) ion-acoustic features propagating in the flowing (v_f) plasma

$$\Delta\omega_\pm = \omega_0 \pm \omega_\pm = \pm c_s k + \mathbf{v}_f \cdot \mathbf{k}, \quad (3)$$

where $\mathbf{k} = \mathbf{k}_s - \mathbf{k}_0$, $c_s \approx \sqrt{ZT_e/M}$ is the sound speed, Z is the average ionization state, M is the ion mass, and the ± sign is used for the red- (−) and blue-shifted (+) solutions.

In a plasma with a component of the flow parallel to the ion-acoustic waves, an asymmetry in the ion-acoustic peak amplitudes is introduced by the range of wave vectors probed by the instrument. The source of this amplitude asymmetry is a result of the asymmetry in the frequency shifts introduced by the first term on the right hand side of Eq. (3), which corresponds to the propagation of ion-acoustic waves. This term causes the corresponding red- and blue-shifted features to shift by different magnitudes when the length of the ion-acoustic wave vector is varied. When averaging the spectrum generated by the range of wave vectors, the spectral feature with the wider range of frequencies results in a lower relative amplitude. For example, consider the case $v_f = c_s$, resulting in $\Delta\omega_\pm = c_s\,(k \pm k)$. In this case, the frequency shift of the red-shifted feature ($\Delta\omega_- = 0$) is not sensitive to the wave vector and will experience no broadening due to finite wave vectors of the diagnostic (at least in the plane of scattering). The blue-shifted feature ($\Delta\omega_- = 2c_s k$) will experience a range of frequencies proportional to the range of wave vectors, and its amplitude will be reduced. This effect was quantified by calculating a weighted series of Thomson-scattering spectra with the necessary range of scattering angles.

To correct for the wavelength-dependent transmission of the low-resolving power system, the spectral response was measured by passing light from a broadband light emitting diode light source with a known spectral output through the diagnostic to determine the spectral sensitivity of the system [Fig. 3(a)]. At the long-wavelength end of the spectrum, the transmission of the system was dominated by the sensitivity of the S-20 photocathode in the streak camera. A notch filter was used to block light scattered around 530 nm. Figure 3(b) shows a measured Thomson-scattering spectrum that sits on a background of bremsstrahlung emission emitted from the plasma and the light Thomson-scattered from the 351-nm drive beams. A background [Fig. 3(c)] was established at each location by turning off the Thomson-scattering probe beam, which was subtracted from each of the corresponding spectra.

III. THOMSON SCATTERING

Figure 4 shows the measured time-resolved Thomson-scattering spectra from electron-plasma and ion-acoustic waves at all five measurement locations along the target normal. The wavelength separation of the electron-plasma wave features, primarily given by the electron plasma frequency ($\omega^2_{pe} = n_e e^2/\varepsilon_0 m_e$), increases with time, indicating that the electron density increases during the laser pulse. The density is lower farther away from the target as suggested by the

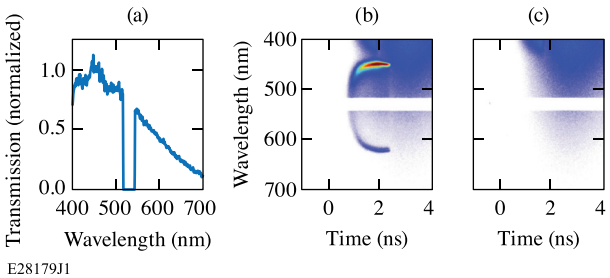

FIG. 3. (a) The measured spectral response of the Thomson-scattering diagnostic. Thomson-scattering data were corrected for the wavelength-dependent transmission. (b) Raw Thomson-scattering spectrum from electron-plasma waves located 1300 μm from the initial target surface. (c) The experiment was repeated without the probe beam to measure the background signal from bremsstrahlung emission and Thomson scattering from the drive beams. The background spectra were used to isolate the Thomson-scattering signal and accurately resolve the relative amplitudes of scattering features.

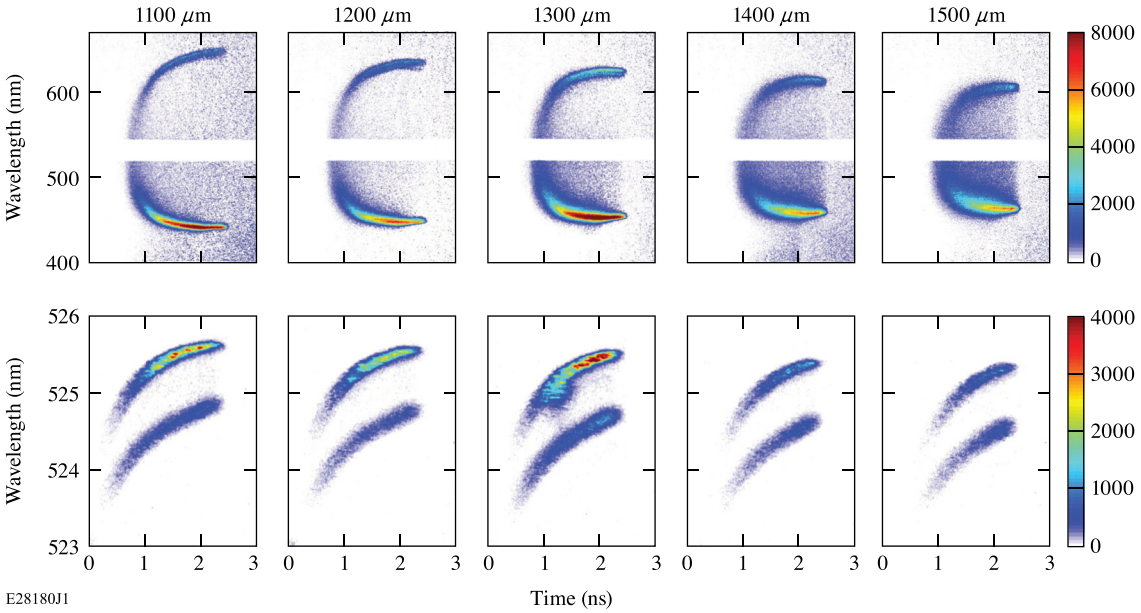

FIG. 4. Time-resolved Thomson-scattering spectra from electron-plasma waves (top row) and ion-acoustic waves (bottom row) are shown at five locations along the target normal. The background signal was removed, and the spectra were corrected for the diagnostic spectral response.

decrease in the wavelength separation between the electron-plasma wave features. The separation between the ion-acoustic wave features is proportional to the sound speed, while the frequency shift of both features results from the global plasma motion. In each image, the ion-acoustic features shift from short to long wavelengths, indicating that the plasma flow velocity decreases with time. The separation between the features was nearly constant in both time and space, indicating that there was little change in the sound speed over the time and space observed by the experiments.

A. Thomson-scattering theory

The calculated Thomson-scattered power spectrum per unit solid angle $d\Omega$ and scattered frequency $d\omega_s$ is given by[40]

$$P_s(\mathbf{R},\omega_s)d\omega_s d\Omega = P_i r_0^2 L d\Omega \frac{d\omega_s}{2\pi}\left(1+\frac{2\omega}{\omega_i}\right) n_e S(\mathbf{k},\omega), \quad (4)$$

where P_i is the incident power of the probe beam, L is the length of the scattering volume, and r_0 is the classical electron radius. The collisionless spectral density function is given by[40]

$$S(\mathbf{k},\omega) = \frac{2\pi}{k}\left|1-\frac{\chi_e}{\varepsilon}\right|^2 f_e\left(\frac{\omega}{k}\right) + \frac{2\pi Z}{k}\left|\frac{\chi_e}{\varepsilon}\right|^2 f_i\left(\frac{\omega}{k}\right), \quad (5)$$

where χ_e and χ_i are the electron and ion susceptibility, f_e and f_i are the normalized, 1-D electron and ion velocity distribution functions projected along the target normal ($f(\mathrm{v}) = \int f^{3D}(\mathbf{v})d\mathrm{v}_\perp$ where $\mathrm{v}_\perp$ is the velocity component perpendicular to the target normal), $\varepsilon = 1 + \chi_e + \chi_i$ is the dielectric function, and[41]

$$\chi_e(\mathbf{k},\omega) = \int_{-\infty}^{\infty} d\mathbf{v}\frac{4\pi e^2 n_e}{m_e k^2}\frac{\mathbf{k}\cdot\partial f_e/\partial\mathbf{v}}{\omega-\mathbf{k}\cdot\mathbf{v}-i\gamma}, \quad (6)$$

is the electron susceptibility. The dependence of the power scattered into the electron-plasma wave feature on the electron distribution function can be seen by evaluating Eq. (5) in the limit where the electron-plasma wave phase velocity (v_ϕ) is much greater than the thermal velocity

$$P_{peak} \propto \left.\frac{f_e(\mathrm{v})}{[df_e(\mathrm{v})/d\mathrm{v}]^2}\right|_{\mathrm{v}=\mathrm{v}_\phi}. \quad (7)$$

The Thomson-scattering data were fit at each measurement location to determine the electron temperature, density, and heat flux. Figure 5 shows electron-plasma and ion-acoustic wave Thomson-scattering spectra fit with the spectra calculated using Maxwellian and non-Maxwellian electron distribution functions. The failure of Maxwellian distributions to recover the relative amplitude and shapes of scattering features was consistent with effects due to heat flux[42] and shows the need for electron distribution functions that include effects of heat flux.

A χ^2 approach[43] was used to measure the plasma parameters and determine the statistical uncertainty of these measurements. The χ^2 test utilized a least-squares calculation normalized to the variance of the data to test the difference between the measurements and the calculated scattered power

$$\chi^2 = \sum_{i=1}^{n}\frac{(D_i - P_i)^2}{\sigma_i^2}, \quad (8)$$

where D_i is the measured Thomson-scattering spectrum and σ_i^2 is the variance in the data at the ith bin over n bins. A bin corresponds to a pixel along the wavelength direction on the detector. The spectrum was calculated on the same wavelength grid as the measurements. The variance was assumed to follow Poisson statistics ($\sigma_i^2 = D_i$).

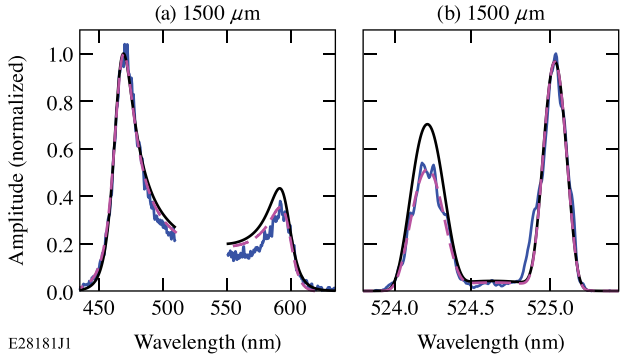

FIG. 5. Measured (blue curves) and calculated (dashed–dotted curves) Thomson-scattering spectra from (a) electron-plasma waves and (b) ion-acoustic waves are shown at $t = 1.5$ ns into the drive pulse. A Spitzer–Härm electron distribution function [Eq. (1)] was used to match the locations, widths, and relative amplitudes of the scattering features. Spectra calculated using a Maxwellian distribution (black curves) do not recover the relative amplitudes of the measurements. All the calculated spectra include instrument effects (e.g., finite collection, spectral instrument function, and instrument sensitivity).

The measured plasma conditions were obtained using the electron-plasma wave spectra by adjusting the plasma parameters (T_e, n_e, λ_{ei}/L_T, and T_i) until a minimum χ^2 value was found (χ^2_{min}). The uncertainty in these measurements was determined by the rate of increase in χ^2 values from the minimum value. The statistical uncertainty in the measurement was determined by the distribution of χ^2 values across the number of fitting parameters p ($p = 3$ and $p = 2$ for electron-plasma and ion-acoustic features, respectively), with the desired confidence level $C = 0.68$. The region of parameter space with χ^2 values within Δ of χ^2_{min} determined the statistical uncertainty[44]

$$\Delta(C,p) = \int_0^C \frac{t^{(p-2)/2}e^{-t/2}}{2^{p/2}\Gamma(p/2)}\,dt, \tag{9}$$

where $\Gamma(z) = \int_0^\infty x^{z-1}e^{-x}dx$ is the gamma function. This analysis resulted in statistical uncertainties of approximately 1% in both electron temperature and density measurements. The absolute error was determined by uncertainties in the diagnostic calibration and was dominated by the spectral dispersion and resolution. These uncertainties were quantified during the calibration of the diagnostic. The spectra were refit after varying the fit parameters within diagnostic uncertainties and resulted in an absolute error of 3% and 2% in the electron temperature and density measurement, respectively.

B. Measured plasma conditions

1. Electron-plasma wave spectrum

Figure 6 shows measurements of the electron temperature, density, and $\lambda_{ei}/|L_T|$. The blue-shifted electron-plasma wave Thomson-scattering feature was used to determine the temperature and density, and the relative amplitudes of the electron-plasma wave features were used to determine λ_{ei}/L_T. The error bars on the data points correspond to the relative (statistical) uncertainty obtained using a χ^2 approach. The low statistical uncertainty is due to the high signal-to-noise ratio in the Thomson-scattering spectra, which can be seen from the measured spectral profiles (Fig. 5). The insets in Figs. 6(a) and 6(b) show the typical absolute error in the electron temperature and density, respectively.

The electron–ion mean free path and temperature-scale length were calculated from the measured plasma conditions. A fifth-order polynomial was fit to the temperature measurements to determine the temperature gradient. To determine the uncertainty in the temperature gradient, the measured temperatures were varied within their relative uncertainties and each combination was fit with a fifth-order polynomial. The standard deviation of the slopes at each location was taken as the uncertainty in the temperature gradient, resulting in error bars of approximately 10%. Uncertainties in calculated quantities (i.e., thermal conductivity, electron–ion mean free path, temperature scale length, and classical heat flux) were determined using standard error propagation with the absolute uncertainty in electron temperature and density.

2. Ion-acoustic wave spectrum

Figure 7 shows ion-acoustic wave spectra and various effects on the relative amplitudes of the ion-acoustic spectra. When the damping

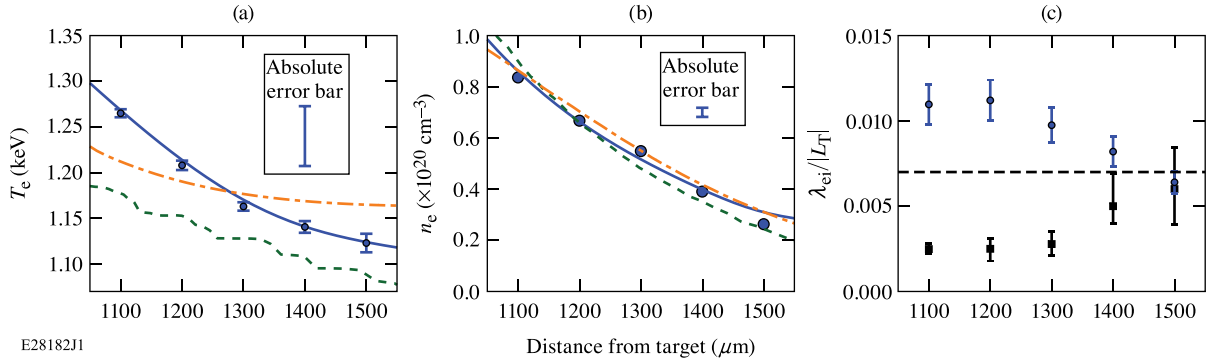

FIG. 6. (a) Electron temperature and (b) density measurements (points) are shown at $t = 1.5$ ns. Plasma profiles from *FLASH* simulations (dashed–dotted orange curve) and 2-D *Troll* calculations using the SNB model (dotted green curve) are included, as well as profiles used in Vlasov–Fokker–Planck and SNB calculations (solid curve). (c) Measurements of the ratio of the electron–ion mean free path to temperature scale length using the measured plasma parameters (blue points) and from fitting Thomson-scattering spectra with Spitzer–Härm distribution functions (black squares) are shown. The theoretical maximum value $\lambda_{ei}/|L_T| = 0.007$ for the Spitzer–Härm theory to be valid (dashed black line) is shown.

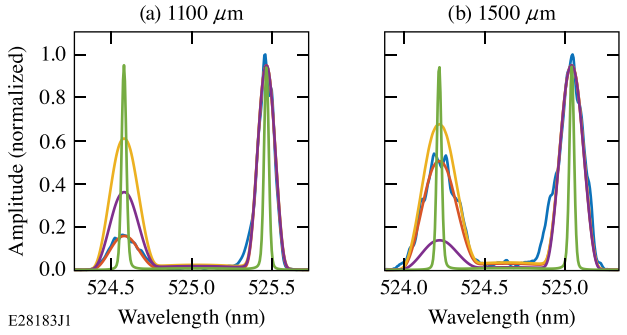

FIG. 7. Measured (blue curves) and calculated Thomson-scattering spectra from ion-acoustic waves are shown (a) 1100 μm and (b) 1500 μm from the initial target surface at $t = 1.5$ ns. Spectra calculated using Maxwellian electron distribution functions without instrument functions (green curves), Maxwellian distributions including wave-vector broadening (yellow curves), Spitzer–Härm distribution functions used to fit the electron-plasma wave features [$\lambda_{ei}/|L_T|(1100\,\mu m) = 5.8 \times 10^{-3}$, $\lambda_{ei}/|L_T|(1500\,\mu m) = 1.5 \times 10^{-3}$] (purple curves), and Spitzer–Härm distributions with $\lambda_{ei}/|L_T|(1100\,\mu m) = 2.5 \times 10^{-3}$, $\lambda_{ei}/|L_T|(1500\,\mu m) = 6.7 \times 10^{-3}$ fit to match the ion-acoustic wave spectrum (red curves). All curves except the green curve include the instrument function, which is dominated by wave-vector broadening.

of the ion-acoustic wave is dominated by electron Landau damping, the relative amplitude of these features is sensitive to the shape of the electron distribution function near the ion-acoustic phase velocities. In these experiments, the electron Landau damping was designed to dominate the ion-wave damping, and the amplitudes were expected to be sensitive to changes in the electron distribution function driven by the return current. As expected, calculations that use Maxwellian distribution functions fail to reproduce the shape of the measured ion-acoustic wave spectrum. The asymmetry in the features calculated with Maxwellian distribution functions is a result of the finite wave vectors (see Sec. II B). For the measurement closest to the target [Fig. 7(a)], the value of $\lambda_{ei}/|L_T|$ required to reproduce the measured electron-plasma wave features with Spitzer–Härm electron distribution functions [Eq. (1)] resulted in a smaller asymmetry in the ion-acoustic wave features than in the data, while farthest from the target [Fig. 7(b)], the value of λ_{ei}/L_T determined from the electron-plasma wave features results in an ion-acoustic wave asymmetry that is too large. This implies that the Spitzer–Härm distribution functions obtained from the electron-plasma features are not correct over the velocity range corresponding to the phase velocity of the ion-acoustic waves. A good fit was obtained by arbitrarily adjusting $\lambda_{ei}/|L_T|$ in Eq. (1) to match the amplitudes of the ion-acoustic wave–scattering features, but this electron distribution function does not simultaneously reproduce the electron plasma wave spectrum at the corresponding locations.

Collisional damping can also affect the amplitude of ion-acoustic wave Thomson-scattering features and it is not included in the spectral density function [Eq. (5)]. For $k_{ia}\,\lambda_{ii} \ll 1$, where k_{ia} is the wave number of the ion-acoustic wave and λ_{ii} is the ion–ion collision mean free path, ions have a short mean free path relative to the wave number, and the collisional damping dominates over the collisionless (Landau) damping. As ZT_e/T_i increases, ion Landau damping of ion-acoustic waves decreases as the phase velocity extends into the tail of the ion distribution function, while electron Landau damping remains relatively constant. For $ZT_e/T_i \approx 16$, ion collisional damping of ion-acoustic waves is comparable to electron Landau damping in the $k_{ia}\lambda_{ei} \approx 1$ regime.[45] In these experiments, a fully ionized aluminum plasma with $T_e/T_i \gtrsim 2$ resulted in $ZT_e/T_i \gtrsim 26$ and $k_{ia}\,\lambda_{ii} \approx 0.5$. The ion collisional damping in this regime was larger than electron Landau damping of ion-acoustic waves, and both were much larger than ion Landau damping. These sources of damping and asymmetry made it difficult to isolate the relative amplitudes of ion-acoustic scattering features from changes in the electron distribution function caused by heat flux.

IV. RESULTS

A. Classical heat flux

The ratio of the electron–ion mean free path to the temperature scale length was determined in two ways: (1) by varying λ_{ei}/L_T in Eq. (1) to recover the relative amplitude of the electron-plasma wave features and (2) by calculating the thermal conductivity and temperature scale length [Eq. (2)] from the measured plasma conditions (see Sec. III B 1). Figure 6(c) compares the values of $\lambda_{ei}/|L_T|$ calculated using the measured plasma parameters [Eq. (2)] with those determined from the fit [Eq. (1)] to the Thomson-scattering electron-plasma wave features. The comparison of $\lambda_{ei}/|L_T|$ determined in these two ways provides an experimental test of the validity of the classical Spitzer-Härm heat flux model. When the two measurements agree, the Spitzer-Härm electron distribution function [Eq. (1)] reproduces the measured Thomson-scattering spectrum and is consistent with the heat flux determined by the measured plasma conditions [Eq. (2)]. When this comparison fails, the electron distribution function required to reproduce the Thomson-scattering spectrum is not consistent with the heat flux determined from the plasma conditions.

Far from the target (1500 μm), both measurements of $\lambda_{ei}/|L_T|$ are in agreement [Fig. 6(c)], indicating that classical thermal transport is a good model for calculating the heat flux in this regime. Figure 8 shows that the Thomson-scattering spectra [Eq. (4)] calculated using classical thermal transport theory [Eq. (1)] recover the relative amplitudes of the

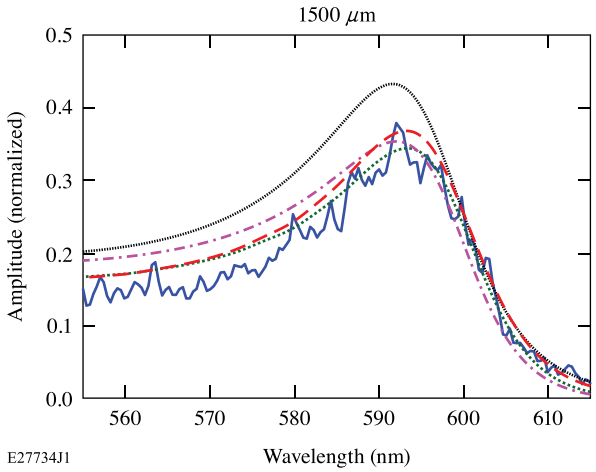

FIG. 8. Thomson-scattering spectra calculated using distribution functions from 1-D Vlasov–Fokker–Planck (red line) and 1-D SNB calculations (green); the Spitzer–Härm model (dot–dashed) and Maxwellian distribution (black) functions are compared with the spectra measured (blue) 1500 μm from the target. The spectra are normalized to the blue-shifted scattering feature. The red-shifted scattering feature is isolated to show the ability of these non-Maxwellian distribution functions to recover the relative amplitudes of scattering features.

data but fail to match the shape of the scattering spectrum far from the resonance (e.g., 550 nm–580 nm). This implies that although the Spitzer–Härm distribution function is a reasonable approximation near the phase velocity of the electron-plasma wave, it is not correct at significantly lower velocities.

For larger relative temperature gradients, the two measurements of $\lambda_{ei}/|L_T|$ diverge [Fig. 6(c)]. This discrepancy indicates an inconsistency between the classical electron distribution function [Eq. (1)] used to fit the Thomson-scattering spectrum and the classical heat flux inferred from the plasma conditions [Eq. (2)]. This result experimentally demonstrates that in plasmas with steep relative temperature gradients ($\lambda_{ei}/|L_T| > 7 \times 10^{-3}$), the classical thermal transport model is not valid.

B. Nonlocal heat flux (VFP)

Discrepancies in $\lambda_{ei}/|L_T|$ measurements [Fig. 6(c)] closer to the target demonstrate that the electron distribution functions in this regime must include the effects of nonlocal thermal transport. To ensure that the nonlocal electron distribution functions were consistent with the measured electron temperature and density at all locations, Vlasov–Fokker–Planck (VFP) calculations using the K2 model[18] were initialized so that over a few collision times the electron distribution functions relaxed to reproduce the measured plasma parameters across the entire measurement region. The electron distribution function, represented as a series of Legendre polynomials $f(t,x,\mathbf{v}) = \sum_n f_n(t,x,\mathrm{v})P_n(\theta)$, where x is the direction along the target normal, were then extracted at each measurement location and used to calculate the scattering spectra. Polynomials up to and including f_8 were used to resolve the distribution function at the measured electron-plasma wave phase velocities. The simulation region had a length of 5 mm, where the measurement region was located between $z = 1.1$ mm and $z = 1.5$ mm as in the experiments. The boundary conditions included a plateau of electron temperature at the higher temperature end of the measurement region ($z < 1$ mm). The extended plasma profiles were required to account for nonlocal contribution to heat flux outside the measurement region. The value of the electron temperature plateau was varied from 1.2 to 2 keV in different runs. The boundary condition (1.8 keV) that generated the Thomson-scattering spectra with the best match across all five locations was used to determine the heat flux.

Figure 9 shows the calculated spectra that best fit the data when using the Vlasov–Fokker–Planck distribution functions. The calculated spectra show good agreement with the relative amplitudes of the measurements, suggesting that the distribution functions are well represented by the Vlasov–Fokker–Planck model around the phase velocity of the electron-plasma wave resonances. At the most-collisional location, Thomson-scattering spectra determined using nonlocal electron distribution functions from Vlasov–Fokker–Planck calculations result in an improved fit to the data compared to using the Spitzer–Härm model over the entire spectrum (Fig. 8).

Figure 10 shows the heat-flux measurements at t = 1.5 ns into the drive pulse. The measured heat-flux values obtained using nonlocal electron distribution functions were lower than those obtained using classical theory near the target where the temperature gradient was the largest. This difference was smaller farther from the target as $\lambda_{ei}/|L_T|$ decreases. The measurements agree at 1500 μm where classical theory was shown to be valid.

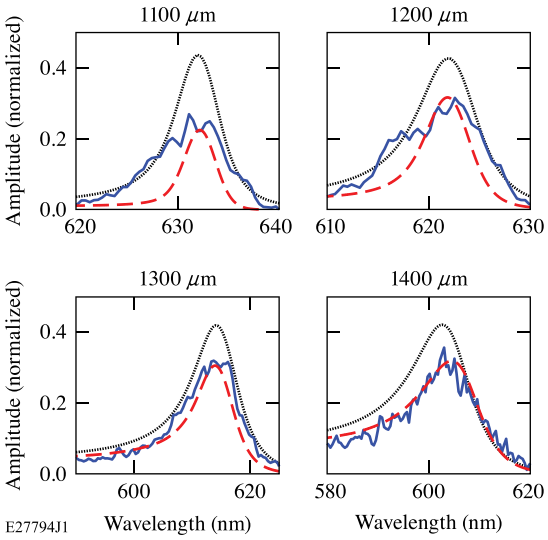

FIG. 9. Measured red-shifted Thomson-scattering features (blue line) are shown at four locations along the target normal. The calculated spectra are shown using electron distribution functions from Vlasov–Fokker–Planck calculations (red) and Maxwellian distribution functions (black). The amplitudes of these spectra are normalized to the peak of the blue-shifted feature.

C. Nonlocal heat flux (SNB)

Similar calculations as described in Sec. IV B were performed using the SNB model.[18] The SNB model uses velocity-dependent mean free paths to include effects of nonlocal thermal transport. Multigroup diffusion allows bins with larger energy to travel farther before undergoing collisions. The heat flux is determined by the

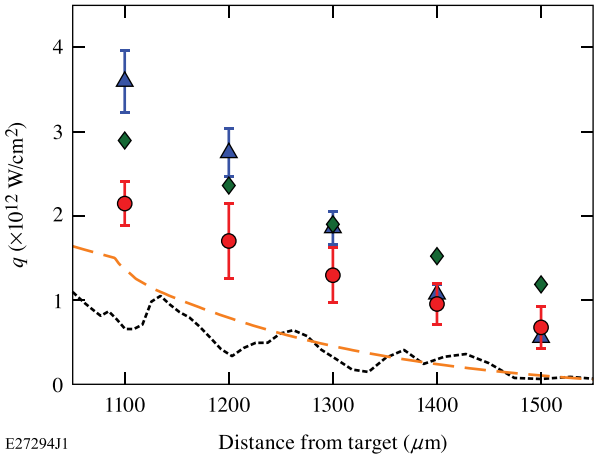

FIG. 10. Heat-flux measurements (red dots) are shown at $t = 1.5$ ns after the start of the $\lambda_{3\omega}$ beams. Classical heat-flux values determined from the measured plasma parameters (blue triangles) are included along with the results from full-scale SNB (dotted black line) and *FLASH* (orange line) simulations and 1-D SNB calculations using the measured plasma profiles (green diamonds). The *FLASH* results underpredict the heat flux due to the flatter temperature profile compared to the measurements [Fig. 6(a)].

deviation from the Spitzer–Härm value due to the range of electron–ion mean free paths.

Figure 10 shows that these 1-D calculations resulted in heat flux reduced from classical values, but still larger than the nonlocal measurements. These calculations also provided electron distribution functions at each measurement location (Fig. 8). Thomson-scattering spectra calculated using the SNB model at the most collisional location had better agreement with the data across the complete spectrum compared to classical theory and were in comparable agreement with the measurements as compared to the spectra determined using the nonlocal electron distribution function from Vlasov–Fokker–Planck calculations. This suggests that in this regime, the SNB model accurately captures the electron distribution function over a wide range of velocities. In regions of larger temperature gradients, distribution functions determined from the 1-D SNB calculation were negative near the Thomson-scattering resonances, and a comparison between the scattering spectra could not be made. This result shows the need to include physics often missing from reduced models. For example, including using high-order polynomials to accurately resolve the electron distribution function are higher velocities ($\sim 3.5\ v_{te}$).

V. SIMULATIONS

A. Classical simulations

Figure 6 shows the simulated electron temperature and density profiles determined by full-scale hydrodynamic simulations using the code *FLASH*.[46] *FLASH* uses a flux-limited thermal transport model that limits the heat flux to the minimum of the classical value [Eq. (2)] and a fraction (f) of the local free-streaming flux ($q_{FS} = n_e T_e v_{te}$). In this simulation, the flux limiter was $f = 0.06$. While the simulated density values are in good agreement with the measurements, the simulated temperature profile is flatter than the measured temperature values. Simulations performed with small flux limiters ($f = 0.04$; $f = 0.05$) predicted steeper electron temperature profiles, but temperature values are noticeably larger than the measurements. A single flux limiter was not able to reproduce the measured temperature and temperature gradient simultaneously.

B. Nonlocal simulations

Figure 6 shows electron temperature and density profiles simulated in 2-D with the radiative hydrodynamic code *Troll*.[33] The *Troll* simulations are in good agreement with the measured electron density and agree with the measured electron temperature within the absolute error bars farther from the target. These simulations underestimate the heat flux at all measured locations (Fig. 10) due to discrepancies in the electron temperature profile, which are dominated by laser deposition near the critical surface [Fig. 6(a)].

VI. CONCLUSIONS

Thomson-scattering spectra were used to measure heat flux. Probing electron-plasma waves with phase velocities of electrons that carry thermal energy down the temperature gradient resulted in a noticeable change in the Thomson-scattering spectra due to the deviation of the electron distribution function from a Maxwellian. This work spanned conditions where classical theory was valid ($\lambda_{ei}/|L_T| < 7 \times 10^{-3}$) and where the electron–ion mean free path was too large for heat flux to be described as a local process. In the region where the plasma was not collisional enough for classical thermal transport theory to be valid ($\lambda_{ei}/|L_T| > 7 \times 10^{-3}$), the measured heat flux was reduced from classical values [Eq. (2)] determined from measured plasma conditions, consistent with nonlocal thermal transport. The heat flux was measured by recovering the relative amplitudes of measured Thomson-scattering spectra using electron distribution functions obtained from Vlasov–Fokker–Planck calculations that included nonlocal effects and maintained the measured plasma profiles. In the most-collisional region, the classical expression for heat flux agreed with the measurement.

Simulations that used a reduced nonlocal[17] or a flux-limited[46] thermal transport model resulted in discrepancies from the measurements of heat flux. Calculations that used the SNB nonlocal model and were self-consistent with the measured plasma electron temperature and density resulted in heat flux values larger than the measurements and show the need to examine the approximations made from the Vlasov–Fokker–Planck model to be computationally efficient. Calculating Thomson-scattering spectra using non-Maxwellian distribution functions can be extended beyond thermal transport studies to investigate various plasma effects that distort the distribution function (e.g., Langdon effect[47] and laser–plasma instabilities[42]).

ACKNOWLEDGMENTS

This work was supported by the U.S. Department of Energy under Cooperative Agreement No. DE-NA0001944, the University of Rochester, and the New York State Energy Research and Development Authority. M.S. contribution to this work was performed under the auspices of the U.S. Department of Energy by LLNL under Contract No. DE-AC52-07NA27344. The support of DOE does not constitute an endorsement of the views expressed in this article.

This report was prepared as an account of the work sponsored by an agency of the U.S. Government. Neither the U.S. Government nor any agency thereof, nor any of their employees, makes any warranty, express, or implied, or assumes any legal liability or responsibility for the accuracy, completeness, or usefulness of any information, apparatus, product, or process disclosed, or represents that its use would not infringe privately owned rights. Reference herein to any specific commercial product, process, or service by trade name, trademark, manufacturer, or otherwise does not necessarily constitute or imply its endorsement, recommendation, or favoring by the U.S. Government or any agency thereof. The views and opinions of the authors expressed herein do not necessarily state or reflect those of the U.S. Government or any agency thereof.

REFERENCES

[1] J. Nuckolls, L. Wood, A. Thiessen, and G. Zimmerman, Nature **239**, 139 (1972).
[2] K. A. Brueckner and S. Jorna, Rev. Mod. Phys. **46**, 325 (1974).
[3] J. D. Lindl, P. Amendt, R. L. Berger, S. G. Glendinning, S. H. Glenzer, S. W. Haan, R. L. Kauffman, O. L. Landen, and L. J. Suter, Phys. Plasmas **11**, 339 (2004).
[4] R. S. Craxton, K. S. Anderson, T. R. Boehly, V. N. Goncharov, D. R. Harding, J. P. Knauer, R. L. McCrory, P. W. McKenty, D. D. Meyerhofer, J. F. Myatt, A. J. Schmitt, J. D. Sethian, R. W. Short, S. Skupsky, W. Theobald, W. L. Kruer, K. Tanaka, R. Betti, T. J. B. Collins, J. A. Delettrez, S. X. Hu, J. A. Marozas, A. V. Maximov, D. T. Michel, P. B. Radha, S. P. Regan, T. C. Sangster, W. Seka, A. A. Solodov, J. M. Soures, C. Stoeckl, and J. D. Zuegel, Phys. Plasmas **22**, 110501 (2015).
[5] C. A. Back, D. H. Kalantar, R. L. Kauffman, R. W. Lee, B. J. MacGowan, D. S. Montgomery, L. V. Powers, T. D. Shepard, G. F. Stone, and L. J. Suter, Phys. Rev. Lett. **77**, 4350 (1996).

[6]A. R. Bell, Phys. Fluids **28**, 2007 (1985).
[7]T. Ditmire, E. T. Gumbrell, R. A. Smith, A. Djaoui, and M. H. R. Hutchinson, Phys. Rev. Lett. **80**, 720 (1998).
[8]E. M. Epperlein and R. W. Short, Phys. Fluids B **3**, 3092 (1991).
[9]D. H. Froula, J. S. Ross, B. B. Pollock, P. Davis, A. N. James, L. Divol, M. J. Edwards, A. A. Offenberger, D. Price, R. P. J. Town, G. R. Tynan, and S. H. Glenzer, Phys. Rev. Lett. **98**, 135001 (2007).
[10]V. N. Goncharov, O. V. Gotchev, E. Vianello, T. R. Boehly, J. P. Knauer, P. W. McKenty, P. B. Radha, S. P. Regan, T. C. Sangster, S. Skupsky, V. A. Smalyuk, R. Betti, R. L. McCrory, D. D. Meyerhofer, and C. Cherfils-Clérouin, Phys. Plasmas **13**, 012702 (2006).
[11]G. Gregori, S. H. Glenzer, J. Knight, C. Niemann, D. Price, D. H. Froula, M. J. Edwards, R. P. J. Town, A. Brantov, W. Rozmus, and V. Y. Bychenkov, Phys. Rev. Lett. **92**, 205006 (2004).
[12]R. J. Henchen, M. Sherlock, W. Rozmus, J. Katz, D. Cao, J. P. Palastro, and D. H. Froula, Phys. Rev. Lett. **121**, 125001 (2018).
[13]J. F. Luciani, P. Mora, and J. Virmont, Phys. Rev. Lett. **51**, 1664 (1983).
[14]R. C. Malone, R. L. McCrory, and R. L. Morse, Phys. Rev. Lett. **34**, 721 (1975).
[15]J. P. Matte and J. Virmont, Phys. Rev. Lett. **49**, 1936 (1982).
[16]J. H. Rogers, J. S. De Groot, Z. Abou-Assaleh, J. P. Matte, T. W. Johnston, and M. D. Rosen, Phys. Fluids B **1**, 741 (1989).
[17]G. P. Schurtz, P. D. Nicolaï, and M. Busquet, Phys. Plasmas **7**, 4238 (2000).
[18]M. Sherlock, J. P. Brodrick, and C. P. Ridgers, Phys. Plasmas **24**, 082706 (2017).
[19]R. P. J. Town, A. R. Bell, and S. J. Rose, Phys. Rev. E **50**, 1413 (1994).
[20]L. Spitzer and R. Härm, Phys. Rev. **89**, 977 (1953).
[21]J. R. Albritton, E. A. Williams, I. B. Bernstein, and K. P. Swartz, Phys. Rev. Lett. **57**, 1887 (1986).
[22]E. M. Epperlein, G. J. Rickard, and A. R. Bell, Comput. Phys. Commun. **52**, 7 (1988).
[23]M. S. White, J. D. Kilkenny, and A. E. Dangor, Phys. Rev. Lett. **35**, 524 (1975).
[24]V. Y. Bychenkov, V. P. Silin, and S. A. Uryupin, Phys. Rep. **164**, 119 (1988).
[25]S. H. Glenzer, W. Rozmus, V. Y. Bychenkov, J. D. Moody, J. Albritton, R. L. Berger, A. Brantov, M. E. Foord, B. J. MacGowan, R. K. Kirkwood, H. A. Baldis, and E. A. Williams, Phys. Rev. Lett. **88**, 235002 (2002).
[26]D. R. Gray and J. D. Kilkenny, Plasma Phys. **22**, 81 (1980).
[27]D. W. Forslund, J. Geophys. Res. **75**, 17, https://doi.org/10.1029/JA075i001p00017 (1970).
[28]J. Hawreliak, D. M. Chambers, S. Glenzer, A. Gouveia, R. J. Kingham, R. S. Marjoribanks, P. A. Pinto, O. Renner, P. Soundhauss, S. Topping, E. Wolfrum, P. E. Young, and J. S. Wark, J. Phys. B: At. Mol. Opt. Phys. **37**, 1541 (2004).
[29]S. H. Glenzer, W. E. Alley, K. G. Estabrook, J. S. De Groot, M. G. Haines, J. H. Hammer, J.-P. Jadaud, B. J. MacGowan, J. D. Moody, W. Rozmus, L. J. Suter, T. L. Weiland, and E. A. Williams, Phys. Plasmas **6**, 2117 (1999).
[30]D. H. Froula, J. S. Ross, L. Divol, N. Meezan, A. J. MacKinnon, R. Wallace, and S. H. Glenzer, Phys. Plasmas **13**, 052704 (2006).
[31]J. S. Ross, S. H. Glenzer, J. P. Palastro, B. B. Pollock, D. Price, L. Divol, G. R. Tynan, and D. H. Froula, Phys. Rev. Lett. **104**, 105001 (2010).
[32]S. H. Glenzer, W. Rozmus, B. J. MacGowan, K. G. Estabrook, J. D. De Groot, G. B. Zimmerman, H. A. Baldis, J. A. Harte, R. W. Lee, E. A. Williams, and B. G. Wilson, Phys. Rev. Lett. **82**, 97 (1999).
[33]E. Lefebvre, S. Bernard, C. Esnault, P. Gauthier, A. Grisollet, P. Hoch, L. Jacquet, G. Kluth, S. Laffite, S. Liberatore, I. Marmajou, P.-E. Masson-Laborde, O. Morice, and J.-L. Willien, "Development and validation of the troll radiation-hydrodynamics code for 3d hohlraum calculations," Nucl. Fusion (to be published).
[34]T. Boehly, D. Brown, R. Craxton, R. Keck, J. Knauer, J. Kelly, T. Kessler, S. Kumpan, S. Loucks, S. Letzring, F. Marshall, R. McCrory, S. Morse, W. Seka, J. Soures, and C. Verdon, Opt. Commun. **133**, 495 (1997).
[35]T. J. Kessler, Y. Lin, J. J. Armstrong, and B. Velazquez, Proc. SPIE **1870**, 95 (1993).
[36]J. Katz, R. Boni, C. Sorce, R. Follett, M. J. Shoup, and D. H. Froula, Rev. Sci. Instrum. **83**, 10E349 (2012).
[37]A. J. Mackinnon, S. Shiromizu, G. Antonini, J. Auerbach, K. Haney, D. H. Froula, J. Moody, G. Gregori, C. Constantin, C. Sorce, L. Divol, R. L. Griffith, S. Glenzer, J. Satariano, P. K. Whitman, S. N. Locke, E. L. Miller, R. Huff, K. Thorp, W. Armstrong, R. Bahr, W. Seka, G. Pien, J. Mathers, S. Morse, S. Loucks, and S. Stagnitto, Rev. Sci. Instrum. **75**, 3906 (2004).
[38]A. Visco, R. P. Drake, D. H. Froula, S. H. Glenzer, and B. B. Pollock, Rev. Sci. Instrum. **79**, 10F545 (2008).
[39]R. K. Follett, J. A. Delettrez, D. H. Edgell, R. J. Henchen, J. Katz, J. F. Myatt, and D. H. Froula, Rev. Sci. Instrum. **87**, 11E401 (2016).
[40]D. H. Froula, S. H. Glenzer, J. Neville, C. Luhmann, and J. Sheffield, *Plasma Scattering of Electromagnetic Radiation: Theory and Measurement Techniques*, 2nd ed. (Academic Press, Amsterdam, 2011).
[41]J. P. Palastro, J. S. Ross, B. Pollock, L. Divol, D. H. Froula, and S. H. Glenzer, Phys. Rev. E **81**, 036411 (2010).
[42]W. Rozmus, T. Chapman, A. Brantov, B. J. Winjum, R. L. Berger, S. Brunner, V. Y. Bychenkov, A. Tableman, M. Tzoufras, and S. Glenzer, Phys. Plasmas **23**, 012707 (2016).
[43]K. Pearson, London, Edinburgh, Dublin Philos. Mag. J. Sci. **50**, 157 (1900).
[44]M. Lampton, B. Margon, and S. Bowyer, Astrophys. J. **208**, 177 (1976).
[45]M. D. Tracy, E. A. Williams, K. G. Estabrook, J. S. DeGroot, and S. M. Cameron, Phys. Fluids B **5**, 1430 (1993).
[46]B. Fryxell, K. Olson, P. Ricker, F. Timmes, M. Zingale, D. Lamb, P. MacNeice, R. Rosner, J. Truran, and H. Tufo, Astrophys. J. Suppl. Ser. **131**, 273 (2000).
[47]A. B. Langdon, Phys. Rev. Lett. **44**, 575 (1980).